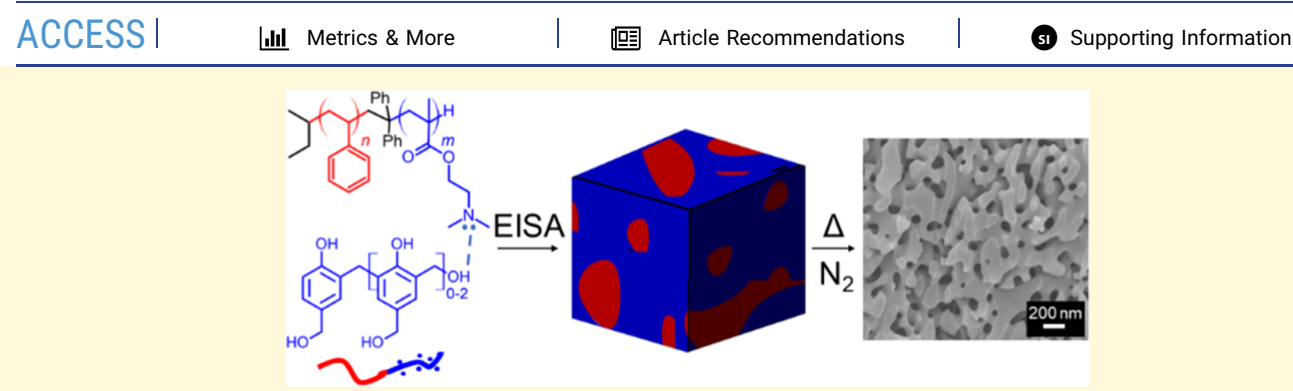


pubs.acs.org/cm Article

# One-Pot Structure Direction of Large-Pore Co-Continuous Carbon Monoliths from Ultralarge Linear Diblock Copolymers

William R. T. Tait, R. Paxton Thedford, Dana V. Chapman, Fei Yu, Judson W. Freidl, Ekaterina S. Sablina, Gavin M. Batsimm, and Ulrich B. Wiesner\*





ABSTRACT: Carbon materials have found ubiquitous use in the fields of electrochemical energy storage (EES) and conversion, due to their electrical and thermal transport properties, typically high specific surface areas, low densities, and stability in a variety of systems. As the demand in particular for increasingly efficient EES devices grows, three-dimensionally (3D) continuous nanostructured electrode materials have gained interest, as they present a pathway to high interfacial areas between electrodes while the overall device has a low areal footprint. Therefore, the development of nanostructured carbon materials with 3D network architectures suited for routes to 3D functional composite materials, e.g., via straightforward backfilling approaches, is an appealing challenge. In this work, two ultralarge pore-size carbons with nonperiodically ordered co-continuous network structures and average pore sizes of 125 nm and 94 nm, respectively, were synthesized using two ultralarge molar mass poly(styrene-block-2-dimethylaminoethyl methacrylate) (PS-b-PDMAEMA, or simply SA) diblock copolymers as structure-directing agents for carbon precursors based on phenol-formaldehyde resols. Careful tuning of a binary solvent system allowed for the avoidance of micellization during evaporation-induced self-assembly of the SA and resols and yielded continuous porous 3D network structures in both carbon and pore spaces upon pyrolysis at higher temperatures of up to 1600 °C, as well as subsequent carbon activation processes. The resulting materials were monolithic and their macroscopic shape and thickness were controllable. These large-pore carbon monoliths may be promising candidates for electrode materials in the future design in particular of 3D continuous EES devices.

## 1. INTRODUCTION

Ordered mesoporous carbon (OMC) materials may find application in a number of technologies related to sustainable energy, including energy storage and conversion devices such as batteries, supercapacitors, and fuel cells. 1-4 As such devices grow in power requirements and shrink in size, a particular challenge has arisen for OMC materials: maximizing active surface area while minimizing areal footprint to yield high areal power densities. Electrochemical energy storage (EES) devices have traditionally been manufactured as layered composites with a two-dimensional (2D) architecture, but the achievement of a three-dimensional (3D) nanoarchitecture in an energystorage device vastly increases areal power density. 5-7 To this end, OMCs are promising candidates for components in nanostructured EES devices. A variety of synthetic routes to OMCs have been developed, generally distinguishable as "topdown" or "bottom-up" methods. Top-down methods include the direct patterning and pyrolysis of carbon precursors via methods such as lithography, but such methods often involve multiple processing steps, expensive equipment, and harsh chemical components. Bottom-up methods such as soft or hard templating and structure direction, in contrast, can be used to define the structure of OMCs through more facile means. In soft templating, a self-assembled soft matter component, such as a polymeric or liquid crystal species, is used to define the architecture of an organic or inorganic component, which is infiltrated after assembly occurs. Through thermal treatments or simple dissolution, the soluble

Received: June 9, 2021 Revised: August 12, 2021 Published: October 1, 2021





or volatile soft matter component can then be easily removed to yield the target OMC. In hard templating, a porous inorganic template is first generated via soft matter self-assembly, which in turn is then used to structure direct the desired OMC. Alternatively, structure-direction strategies involve self-assembling structure-directing agents undergoing co-assembly with a functional precursor to result in a nanocomposite material. This composite can then be processed via thermal treatment to yield a structured functional material.

To the best of our knowledge, the first example of a bottomup route to OMCs was demonstrated by Ryoo et al. 12 A large body of solution-based bottom-up methods for synthesizing mesoporous carbons has been generated since, typically involving the use of small-molecule or oligomeric carbon precursors in tandem with a structure-directing agent such as amphiphilic block copolymers (BCPs). 13-27 BCPs can spontaneously undergo microphase segregation on the mesoscale of tens of nanometers to form various morphologies, most commonly lamellar, close-packed micellar, hexagonally packed cylindrical, or bicontinuous gyroidal phases.<sup>28</sup> A salient feature of BCP self-assembly is the very high degree of tunability; mesoscale structure and periodicity can be tuned by synthetic or processing means: polymer molar mass, block volume fractions, blending with small-molecule additives, or careful selection of solvents. The versatility of BCPs as structure-defining agents along with a wealth of available processing techniques has given rise to diversity of OMC materials. OMCs with a long-range mesoscale order have been synthesized via evaporation-induced self-assembly (EISA) leading to various morphologies with pore diameters ranging from several to tens of nanometers. 13-21 Mesoporous carbons with hierarchical pore structures have also been synthesized from BCP-based methods using processing strategies such as spinodal decomposition, nonsolvent-induced phase separation, and polycondensation. 3,222-27 In all such methods, a particular strength of polymeric species such as BCPs is their amenability to highly scalable solution processing.

While several routes, including some based on OMCs, toward 3D nanoarchitectures in EES devices exist, there is much room for optimization. 7,27,29-32 In previous work from Werner et al., BCP structure direction was employed to create co-continuous cubic gyroidal OMC monoliths, which served as structure-defining graphitic anodes in a 3D lithium-sulfur battery with an interpenetrating anode, separator, and cathode. After the self-limiting electropolymerization of poly(phenylene oxide) (PPO) was used to create a conformal coating/separator of the solid polymer electrolyte on the gyroidal mesoporous carbon, the remaining pore space was filled with a composite cathode consisting of elemental sulfur and conductive poly(3,4-ethylene dioxythiophene) (PEDOT). Upon lithiation, this device held an open circuit potential of 2.8 V and was successfully cycled through charging/ discharging up to 20 times. It thereby demonstrated, to the best of our knowledge for the first time, proof of principle of a fully functional battery with 3D architecture, in which all components interpenetrated each other on the nanoscale with the thickness of each component below 50 nm. But the achieved actual capacity was much lower than its theoretical. Much of this lost capacity was hypothesized to be due to discontinuities in the sulfur/PEDOT phase due to inhomogeneous backfilling or volume expansion during cycling. A part of this issue can be attributed to the high degree of confinement;

the gyroidal anode contained mesopores that were  $\approx$ 40 nm in diameter, which left only  $\approx$ 20 nm diameter pores for backfilling of the cathode phase after the  $\approx$ 10 nm thick coating with the PPO separator was generated. Full homogenous penetration of this small pore space throughout a macroscopic monolith with the thickness of 50–100  $\mu$ m with a sulfur/PEDOT composite cathode was therefore challenging to achieve.<sup>7</sup>

One promising route to overcome these difficulties in an effort to potentially improve the actual achievable capacity of such an interpenetrating self-assembled 3D nanobattery is thus to increase the molar mass of the structure-directing block copolymer used in the self-assembly approach to porous carbon anodes, which would result in larger pores after pyrolysis. In previous work, BCPs with a molar mass on the order of 30-110 kDa were used to synthesize OMCs of pore sizes ranging from 10 to 40 nm. 13 Increasing pore size substantially beyond these mesopore values and into the macropore regime (i.e., with pore sizes >50 nm) requires significantly higher molar mass BCP structure-directing agents, however, as self-assembled domain size does not scale linearly with polymer molar mass (e.g., for lamellar morphologies domain size scales with the polymer molar mass to the power 2/3).<sup>33</sup>

This work demonstrates a one-pot route to co-continuous porous carbons with average pore diameters of 125 and 94 nm, respectively, via ultralarge molar mass (ULMM) linear diblockpolymer self-assembly. Poly(styrene-block-2-dimethylaminoethyl methacrylate)) (PS-b-PDMAEMA, or simply SA) BCPs with a molar mass of order 1000 kDa are synthesized via anionic polymerization and mixed with phenol-formaldehyde resols as a carbon precursor. After EISA in a carefully tuned solvent system of tetrahydrofuran (THF) and ethyl acetate (EA), the hybrid SA/resols solid films are then pyrolyzed at 900 or 1600 °C, respectively, under a nitrogen atmosphere to yield porous carbon monoliths with co-continuous pore structures, referred to as ultralarge porous carbons (ULPCs). The use of ULMM BCPs as structure-directing agents presents a new set of challenges, including increased synthetic complexity and the propensity of the BCPs to micellize in solution, leading to undesired morphologies of the final structures upon self-assembly with resols. Here, solutions are showcased to overcome such issues. Through the achievement of pore diameters in excess of 90 nm in bulk monoliths, while preserving the co-continuous nature of the network structure, this work demonstrates BCP-derived porous carbons with 3D continuous porosity at previously inaccessible length scales, pushing well into the macropore regime via self-assembly mechanisms rather than spinodal decomposition. An increase in the average pore size of the ULPCs correlated with an increase in the molar mass of the ULMM-SA copolymers used as structure-directing agents is also established. With large, accessible 3D pore spaces, as well as microporous carbon walls, these materials are expected to find applications in the improvement of a number of self-assembly-derived nanoarchitectured EES devices.

#### 2. EXPERIMENTAL METHODS

**2.1. Materials.** Styrene, 2-dimethylaminoethyl methacrylate, *n*-butyllithium (2.0 M in hexane), *sec*-butyllithium (1.4 M in cyclohexane), 1,1-diphenylethylene (97%), phenol (redistilled >99%), *p*-toluenesulfonic acid monohydrate, THF (99.9% anhydrous), ACS grade ethyl acetate, sodium hydroxide pellets, di-*n*-

butylmagnesium (1.0 M in heptane), trioctylaluminum (25 wt % in hexanes), phosphorus pentoxide, magnesium sulfate, ACS grade methanol, ACS grade isopropanol, and ACS grade chloroform were purchased from Millipore Sigma. The ethyl acetate was dried over magnesium sulfate and stored over molecular sieves. Methanol was degassed on a Schlenk line via three freeze—pump—thaw cycles and stored in a glovebox. The rest of the chemicals were used in the following protocol, as purchased.

2.2. Polymer Synthesis. ULMM-SA was synthesized via sequential anionic polymerization, using a method adapted from a procedure described elsewhere.<sup>34</sup> One liter of THF was first purified using n-butyllithium, with 1,1-diphenylethylene (DPE) as the indicator. Once the THF solution was colored red, indicating that n-butyllithium had reacted with all protic species and was now forming 1,1-diphenylhexyllithium with the DPE, THF was distilled through a Schlenk line into a 2 L reactor. This reactor was then transferred into a glovebox, where a small amount of DPE was added, followed by dropwise addition of sec-butyllithium, until the solution turned a very light pink. This served to show that the THF was indeed clean. The THF was then allowed to sit at room temperature for 3-4 h, to let any remaining living sec-butyllithium degrade. After this time, the reactor was brought out of the glovebox, chilled to -78 °C in a bath of isopropanol and dry ice, and had nitrogen actively purging through its volume.

The styrene monomer was distilled over di-n-butylmagnesium after three freeze-pump-thaw cycles on a Schlenk line bridge apparatus. Then, sec-butyllithium was added to the reactor as an initiating species through a needle and syringe. The distilled styrene was then added to the THF being kept at -78 °C via cannula transfer. The colorimetric change of the solution to orange was a sign of successful initiation. The styrene was allowed to react for 1-2 h, and then capped with DPE, leaving the active chain end a much more stable carbanion, and turning the solution red. DMAEMA was distilled over trioctylaluminum after three freeze-pump-thaw cycles, also using a bridge on the Schlenk line. The distilled DMAEMA was added to the reactor dropwise through cannula transfer, which caused the solution to turn transparent. The DMAEMA block was allowed to react at a temperature maintained around -50 °C for 1 h, and the reactive chain ends were then quenched with degassed methanol. The polymer solution was concentrated using a rotary evaporator, redissolved in chloroform, and then concentrated again until it had a consistency comparable to honey. The solution was then added dropwise to a flask of stirring methanol, causing the polymer to precipitate out of solution in droplet-sized beads. This precipitate was collected via vacuum filtration and then dried in a vacuum oven overnight at 40 °C with a dish of phosphorus pentoxide in the oven as an additional drying agent

- 2.3. Polymer Characterization. Taking aliquots during synthesis for molar mass determination proved difficult and was likely to terminate at least a fraction of the living chain ends of the anionic polymerization. This combined with the large molar mass being above many columns' resolution and the PDMAEMA block's tendency to cause tailing led to the decision to determine molar mass via Zimm plots rather than gel permeation chromatography. Zimm plots were performed on a Brookhaven SMI-200 goniometer static light scattering system using a 632.8 nm He-Ne laser and an avalanche photodiode detector. Decalin was used as the reservoir solvent with borosilicate glass sample vials. Solutions of concentrations of 0.2, 0.4, 0.6, 0.8, and 1.2 mg/mL were generated in anhydrous THF for Zimm plot analysis to determine the molar mass. Zimm plot analysis was performed twice for each of the two ULMM BCPs (see one data set in the main text and one in the SI). Block fractions were determined employing <sup>1</sup>H NMR (see the results in Figure S2). Dilute samples were prepared in deuterated chloroform for <sup>1</sup>H NMR, and analysis was run on a Bruker AV-500 Automated NMR.
- **2.4. Resols Synthesis.** Phenol-formaldehyde resols with molar mass <500 g/mol were synthesized using the polymerization of phenol and formaldehyde in basic conditions from previously described methods.<sup>13</sup> A synthesis consisted of melting 9.411 g of phenol (0.1 mol) in a flask, equipped with a reflux condenser using air

as the coolant, in a water bath at 45 °C. In parallel, 0.4 g of sodium hydroxide was dissolved in 1.6 g of deionized water, making a 20 wt % solution, which was wholly added dropwise to the melted, stirring phenol. This would result in a solution of sodium phenoxide, which was then stirred for 10 min. Then, 14.89 mL of formalin (37% formaldehyde in water) was added dropwise to the solution over the next 10 min; this was equivalent to adding 0.2 mol of formaldehyde. The solution was heated to 75 °C and held at this temperature to react for 1 h. The solution was then cooled to room temperature and neutralized with the addition of p-toluenesulfonic acid.

This solution was freeze-dried on a Schlenk line for >12 h and then dissolved in THF. This cloudy solution was filtered through a PTFE syringe filter (0.45  $\mu$ m) to remove precipitates, dried again overnight on a Schlenk line, and then dissolved in THF to 20 wt %. The final solution was stored over molecular sieves in a freezer.

- **2.5.** Co-assembly and Pyrolysis. The three parameters considered when designing the co-assembly of the ULMM-SA and the resols were the resols-to-polymer ratio, THF-to-EA ratio, and total weight percent of solids in solution. In a typical sample preparation, the final polymer-resols ratio was 1:1 and the final concentration of the solution was 4 wt % total solids. The solvent system was 70:30 THF:EA and 60:40 THF:EA by mass for ULPC-1 and ULPC-2, respectively. Other ratios of the solvents did produce stable nonperiodically ordered co-continuous carbon monoliths, while the neat solvents never did; however, the optimized ratios given above provided the most reproducible mesostructures with minimized inclusions of spherical residues originating from micellization pathways during evaporation-induced self-assembly. The solution was stirred for at least 12 h once it was prepared. After mixing, the solution was cast into an HDPE or aluminum foil dish, placed on a hotplate at 40  $^{\circ}\text{C}\text{,}$  and covered with a glass dome. A dish containing pure THF, the majority solvent for both ULMM-SA solutions, was also placed under the glass dome on the hotplate to saturate the local environment with THF and further slow the evaporation of the polymer-resols solution. The sample was taken off the hotplate once all signs of condensing solvent were gone from the covering dome, and it was then put into an oven at 130 °C for 12 h. After this curing process, the films were removed from the dishes and put in a tube furnace to pyrolyze at 600 °C for 3 h in a N2 atmosphere (ramp rate 1 °C/min, under flowing N<sub>2</sub>) and then 900 °C for 1 h (ramp rate 3 °C/ min, under flowing N<sub>2</sub>) or 1600 °C for 1 h (ramp rate 5 °C/min, under flowing N<sub>2</sub>). These samples were finally removed from the tube furnace and prepared for various characterizations. Samples to be used for Raman spectroscopy and HR-TEM after higher-temperature thermal treatment were pyrolyzed at 1600 °C for 1 h (ramp rate 5 °C/min, under a N<sub>2</sub> atmosphere).
- **2.6. Scanning Electron Microscopy.** Samples were prepared by creating fresh fractures in monolithic carbon samples and then placing those fracture sides upon carbon tape mounted on a 10 mm SEM stub. The samples were then sputter-coated with gold-palladium and mounted on a shuttle. The samples were analyzed on either a Zeiss Gemini 500 or Tescan Mira3 SEM at 2–3 kV.
- **2.7. Nitrogen Physisorption and Carbon Activation.** Samples were analyzed by a Micromeritics ASAP 2020 surface area and porosity analyzer at  $-196\,^{\circ}$ C. ULPC was added to the sample tube, which was degassed under dynamic vacuum at 120  $^{\circ}$ C for at least 12 h. The sample tubes were then put on the analysis port. ASAP 2020 software was then used to carry out the nitrogen physisorption measurements; Brunauer–Emmett–Teller (BET) analysis was performed to determine surface area, and the Barrett–Joyner–Halenda (BJH) method was employed on the desorption branch of the isotherms to determine pore-size distributions. Subsequently, the same 900  $^{\circ}$ C-pyrolyzed carbon samples for each ULPC were activated at 800  $^{\circ}$ C for 2 h under CO<sub>2</sub>, and post-activation samples were subjected to the same nitrogen physisorption experiments.
- **2.8. Transmission Electron Microscopy.** ULPC samples (1600 °C-pyrolyzed) were ground into a fine powder with a mortar and pestle and suspended in ethanol. These suspensions were then cast over carbon-coated copper grids with a 400 mesh. The prepped

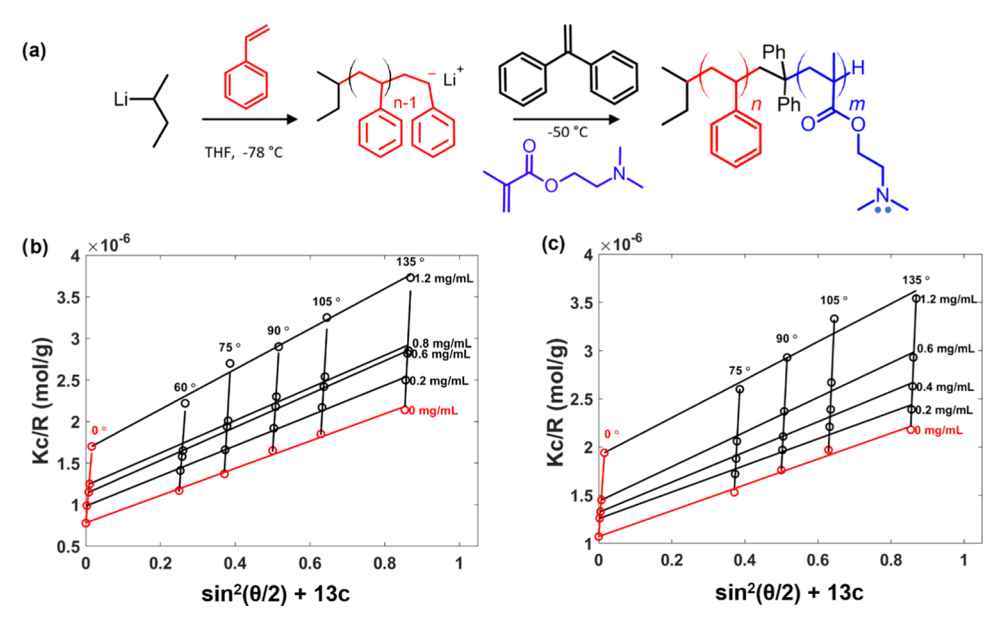


Figure 1. (a) Synthesis scheme for ULMM-SA diblock copolymers. (b, c) Experimental Zimm plots for (b) ULMM-SA1 and (c) ULMM-SA2 used to determine weight average molar mass,  $M_{\rm w}$  (see the main text for details).

samples were analyzed on an FEI-F20 STEM/TEM at an accelerating voltage of 200 kV.

**2.9. Raman Spectroscopy.** Samples were analyzed at room temperature on an InVia Renishaw 500 confocal microscope Raman spectrometer, fitted with a 488 nm diode laser as an excitation source. The laser was focused on the sample with a lens for 50x magnification. Three scans for each 900 °C-pyrolyzed ULPC and four scans for each 1600 °C-pyrolyzed ULPC were taken at 100% power for 10 s, with each scan focused on different spots on the carbon samples, and these results were averaged and normalized via min—max scaling for each scanned sample.

**2.10. X-ray Characterization.** X-ray diffraction data were collected at the Soft Matter Interfaces beamline of the National Synchrotron Light Source, NSLS II. Samples were mounted on scotch tape, and 2D diffraction images were collected using a monochromatic 14 keV energy X-ray beam on a Pilatus 3300 K-W detector at a distance of 0.274 m covering scattering angles ranging from -3.5 to 62°. Individual images collected in this way were then stitched together to form a composite scattering image covering the entirety of the *q*-space and radially integrated using custom python-based analysis code developed at the beamline.

XPS data were collected on a Scienta Omicron ESCA 2SR XPS System. Atomic composition survey spectra were collected at 200 eV pass energy, and HR-XPS were collected at 50 eV pass energy. The samples analyzed were conductive, so no charge neutralization flood gun was used in sample preparation. Data were analyzed using CasaXPS software.

2.11. Four-Point Conductivity Measurements. Quartz substrates were laser cut from 1 mm quartz microscope slides (Electron Microscopy Sciences) into 1 cm squares and etched to have a 100  $\mu$ m deep, 3 × 6 mm channel using a VersaLaser VLS3.50 CO<sub>2</sub> laser (Universal Laser Systems). Carbon samples treated to high temperatures were fixed into the etched channels using Crystalbond 509 and then polished down using diamond lapping films until level with the surrounding quartz substrate. Metal contacts were then deposited onto the sample in a linear four-terminal geometry using a thermal evaporator: a 5 nm chromium adhesion layer followed by a 30 nm gold layer. These gold contact pads were then wire-bonded to a Quantum Design PPMS DC resistivity sample puck and four-point DC resistance measurements were performed using an excitation current of 100  $\mu$ A.

## 3. RESULTS AND DISCUSSION

3.1. Polymer Synthesis and Characterization. SA diblock copolymers were synthesized via living anionic polymerization according to the scheme as shown in Figure 1a. Due to the stoichiometric amount of the sec-butyllithium initiator required per growing polymer chain, the very high degree of polymerization, and the low reactor volumes present in lab-scale methods, the anionic living synthesis for ULMM polymers is made difficult by the high sensitivity of carbanion active species to trace impurities. Less stringent synthesis conditions are typically required for the synthesis of bottlebrush BCPs with ring-opening metathesis polymerization (ROMP), which can reliably produce BCPs with molar mass in excess of 1000 kDa. 35,36 Such bottlebrush BCPs have been used to template carbon precursors via co-assembly and subsequent pyrolysis.<sup>37,38</sup> However, bottlebrush BCPs generally have more restrictive phase windows as compared to linear BCPs, as demonstrated by the micellized morphology of the previous examples. Relatively dense micellar structures limit the ability to yield monolithic and stand-alone organic or inorganic co-continuous structures in the bulk regime from bottlebrush BCPs. Thus, it remains desirable to develop methods for the creation of porous carbons using linear BCPs. While examples of linear BCPs with molar mass in excess of 1000 kDa in the literature are sparse, there have been protocols developed toward this end using anionic living polymer-

To tackle the challenges related to low initiator concentrations being used, the first strategy employed was sizing up the volume of the reactor to the scale of a 1 L synthesis. The solvent used for the entire polymerization was THF. As another consideration to maximize the likelihood of successful polymerization, sec-butyllithium was used as a cleaning agent for the THF prior to monomer addition or initiation; this was doubly helpful, in that the sec-butyllithium would react with and remove impurities, and the lithium salt enolates of acetaldehyde that resulted from the decomposition of THF by sec-butyllithium served to stabilize the chain ends in the polar THF solvent and reduce the free ion concentration.

After the successful synthesis of two ULMM BCPs referred to in the following as ULMM-SA1/SA2, the materials were characterized by light scattering and employing Zimm plots to determine weight average molar mass  $(M_w)$  as well as by  ${}^1H$ NMR to determine the volume fractions of the respective blocks. Zimm plots result from an application of static light scattering analyzed at different angles to solutions of the polymer at different concentrations. The detector output is given as  $Kc/R(\theta, c)$ , and  $K = 4\pi^2 n_0^2 (dn/dc)^2 / (N_A \lambda^4)$ , where  $n_0$  is the refractive index of the solvent, dn/dc is the change in the solution refractive index with change in solution concentration,  $N_A$  is Avogadro's number, and  $\lambda$  is the wavelength of the light source;  $R(\theta, c)$  is the corrected Rayleigh ratio as a function of the detector angle,  $\theta$ , and solution concentration, c. Linear plots of detector output versus  $\sin^2(\theta/2)$  plus an experimentally determined calibration coefficient for each angle,  $\theta$ , and for each tested concentration are then doubly extrapolated down to a zero-degree angle and zero-concentration point (the intersection of the two extrapolated red lines of zero degree and zero angle in Figures 1b,c, S1a, and S1b).<sup>43</sup> Since  $Kc/R(\theta, c) = 1/M_w$  as  $\theta$  and capproach zero, this zero-degree and zero-concentration point can be used to determine weight average molar mass,  $M_{w}$ , of polymers in solution.<sup>43</sup> Since Zimm plots can be sensitive to optical impurities such as dust, two independent sets of Zimm plots were taken for each ULMM-SA BCP to yield averaged M<sub>w</sub> values (Figures 1b,c, S1a, and S1b). Table 1 shows the

Table 1. Polymer Characteristics of BCPs ULMM-SA1 and ULMM-SA2

polymer	$M_{\rm w}~({ m kDa})^a$	$f_{\rm v}  {\rm PS}^{b}$	$f_{\rm v}$ PDMAEMA <sup>b</sup>
ULMM-SA1	$1257 \pm 144$	0.65	0.35
ULMM-SA2	$913 \pm 83$	0.80	0.20

<sup>&</sup>quot;Average values of  $M_{\rm w}$  determined from two separate Zimm plot analyses of the same material. "Volume fractions,  $f_{\rm w}$  determined by <sup>1</sup>H NMR (Figure S2).

results for these averaged  $M_{\rm w}$  values together with the volume fractions,  $f_{\rm w}$ , for the polymers synthesized and used for this work, demonstrating that both BCPs had a molar mass around 1 M kDa, with ULMM-SA1 being the larger copolymer, and a larger PS volume fraction relative to PDMAEMA ( $f_{\rm w}({\rm PS})$ ) of

0.65/0.8 for ULMM-SA1/SA2). For estimates of the degrees of polymerization of each block based on weight average molar mass, see the Supporting Information.

**3.2. BCP and Resols Co-assembly.** To date, a number of applications of ULMM linear BCPs have been in photonics. using lamellar and cylindrical morphologies. 40,41 Furthermore, examples of ULMM BCPs that took advantage of more sophisticated linear BCP phase morphologies did so in the thin-film regime, rather than the bulk, using strategies to accelerate and improve structure formation such as solventvapor annealing.<sup>39,44</sup> Even though ULMM BCPs have been synthesized via living anionic polymerization and their assembly behavior studied in the past, challenges remain in accessing desired morphologies associated with slow structure formation kinetics and associated trapping of intermediate states on the way to equilibrium structures as a result of the large and highly entangled polymer chains. In this vein, the biggest challenge originally faced in the current study was BCP micellization in solution resulting in undesired spherical carbon structures after heat processing (e.g., see the scanning electron microscopy (SEM) image in Figure 2, upper right). This was likely due to several factors that were all intensified by the ultralarge molar mass of the BCPs.  $\chi N$ , the product of the Flory-Huggins polymer-polymer interaction parameter,  $\chi$ , and the degree of polymerization, N (which is proportional to the molar mass), is used as a way to determine the segregation strength of the polymer blocks in a BCP and needs to be sufficiently large for BCPs in the condensed state to transition from the disordered to an ordered state.<sup>39</sup> In ULMM BCPs, the high N makes  $\chi N$  quite large, causing the ULMM-SAs to segregate readily.

Furthermore, while polystyrene and PDMAEMA should both theoretically be soluble in THF and EA (Table 2), the asymmetric nature of the BCP compounded by the fact that larger molar mass requires solute and solvent to have very close solubility parameters to properly dissolve, means that solvents that may work for individual blocks, or even for smaller BCPs of the same composition, may not work for ULMM BCPs. This made the tuning of the solvent system critical to avoid solution micellization. As polar compounds involving hydrogen-bonding-capable functional groups are involved (see Figure 2, left side), Hansen solubility parameters were used to inform solvent system choices.

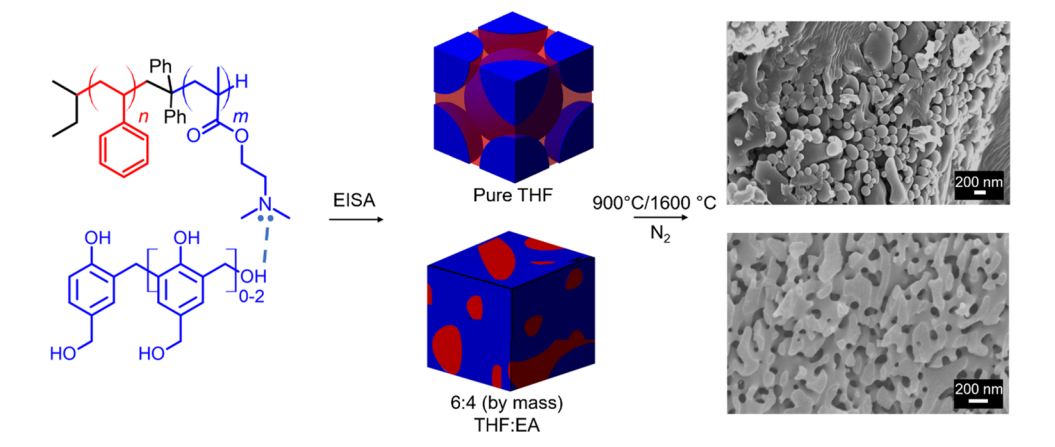


Figure 2. Hydrogen-bonding enhanced co-assembly of SA BCP and resols (left) via EISA from different solvent systems (middle) leads to porous materials with different morphologies after high-temperature treatments (right). The SEM images show representative cross sections from carbons produced via self-assembly pathways dominated by micellization (top) or desired co-continuous structures (bottom).

Table 2. Hansen Solubility Parameters of Solvents, Polymer Blocks, and Resols Used in This Work.  $\delta_{\rm d}$ ,  $\delta_{\rm p}$ , and  $\delta_{\rm h}$  are the Terms for the Dispersive, Polar, and Hydrogen-Bonding Components of the Three-Term Hansen Solubility Parameters.

	$\delta_{ m d}$	$\delta_{ m p}$	$\delta_{ m h}$	$\delta_{t}$
EA <sup>46</sup>	15.8	5.3	7.2	18.2
THF <sup>47</sup>	16.8	5.7	8.0	19.5
polystyrene <sup>45</sup>	21.3	5.8	4.3	22.5
PDMAEMA <sup>b</sup>	12.5	3.4	9.8	16.2
resols <sup>b</sup>	16.0	22.7	12.6	30.5

<sup>a</sup>These can be combined by the equation  $(\delta_{\rm d}^2 + \delta_{\rm p}^2 + \delta_{\rm h}^2)^{0.5} = \delta_{\rm t}$ to obtain a single solubility parameter,  $\delta_v$  analogous to the Hildebrand solubility parameter. All units are in (MPa)<sup>0.5</sup>. <sup>b</sup>Approximated through group contribution method calculations taken from ref 48.

This balancing act only gets more difficult once the phenol-formaldehyde resols are added. The resols not only introduce a new component to interact with both the BCP and the solvent(s), but they are also much more hydrophilic than any of the other components, showing high polar and hydrogen-bonding components,  $\delta_{\rm p}$  and  $\delta_{\rm h}$ , of the Hansen solubility parameters (Table 2). The resols, being hydrogen bond donors, should segregate predominantly to the PDMAEMA block, which has both a dimethylamino group and an ester group as weak hydrogen bond acceptors. This combination, however, will increase the volume fraction of the PDMAEMA block, which is another major factor, in addition to  $\chi N$ , that determines the final morphology of the microphase separation process. Therefore, as resols were added, the BCP-resols composite moved through its phase diagram based on the PDMAEMA/resols volume fraction. 11,49–51 However, due to the massive size of the BCPs, particularly the glassy styrene

block, if the ULMM-SA and resols micellize at any point in the co-assembly process, due to either interactions with the solvent or being moved through a portion of the phase diagram that has micelles, their relaxation times would be so large, they would likely get structurally trapped as a micellar morphology in the bulk.

Hansen solubility parameters for a binary solvent system, AB, can be calculated by 46

$$\delta_{\rm d,AB} = \delta_{\rm d,A} \nu_{\rm a} + \delta_{\rm d,B} \nu_{\rm b} \tag{2}$$

where  $v_i$  is the volume fraction of the binary solvent component i.  $\delta_p$  and  $\delta_h$  for binary solvents can be calculated for binary solvent mixtures in an analogous way. Housing this method, Hansen solubility parameters were calculated for mixtures of EA:THF from 0:100 to 100:0 by mass, with EA increasing by a step size of 10. Hansen solubility parameters can be used to establish a "sphere" of solubility, using  $(2\delta_d, \delta_p, \delta_h)$  as the coordinates for the center of the sphere, which has a radius of  $R_0$ , the "solubility radius". Then, using the values from Table 2, values for  $R_a$ , the distance of the solvent coordinate from the center point of the solute sphere, was calculated by the equation:

$$R_{a}^{2} = 4(\delta_{d,1} - \delta_{d,2})^{2} + (\delta_{p,1} - \delta_{p,2})^{2} + (\delta_{h,1} - \delta_{h,2})^{2}$$
(3)

where subscript 1 identifies parameters for the solvent and subscript 2 identifies parameters for the solute. Typically, if  $R_{\rm a}$  is within the sphere created around the center  $(2\delta_{\rm d}, \delta_{\rm p}, \delta_{\rm h})$  by radius  $R_{\rm 0}$ , one can expect the solvent to dissolve the solute. While  $R_{\rm 0}$  cannot be readily calculated by theoretical methods, and each solute has a different  $R_{\rm 0}$ , in general, the smaller the radius  $R_{\rm a}$ , the more likely the solvent is to dissolve the solute. Figure 3a shows that  $R_{\rm a}$  increases for polystyrene and resols as

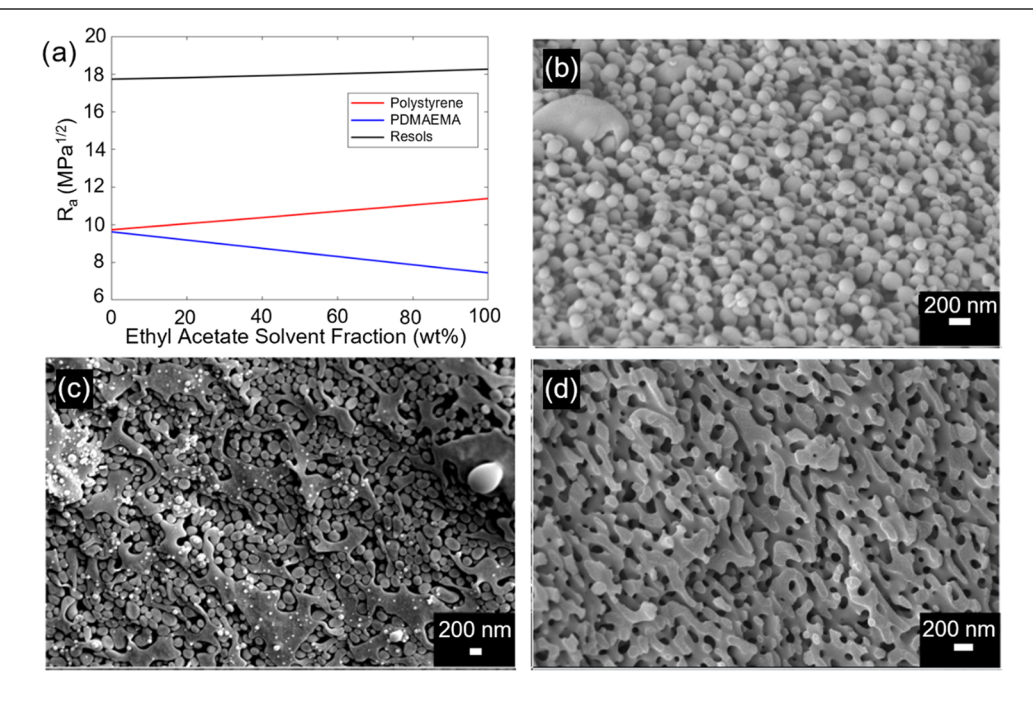


Figure 3. Solubility of SA and resols in various solvent systems. (a) Calculated values of  $R_a$  (from eq 3) of different solutes, as indicated, based on the composition of the THF:EA binary solvent system (see the main text for details). (b–d) Representative SEM images of resulting carbon morphologies after pyrolysis at 900 °C formed from ULMM-SA2 co-assembling with resols in (b) THF, (c) EA, or (d) 6:4 (by mass) mixture of THF:EA, demonstrating vastly different assembly pathways toward the final bulk structure when either single solvents (THF or EA) or binary THF/EA solvent mixtures close to 50:50 composition are used (i.e., micellization versus nonmicellization pathways).

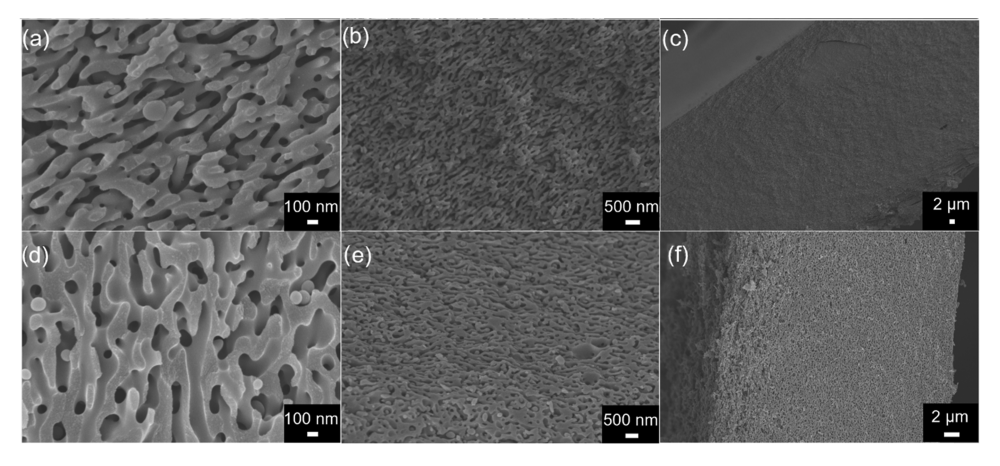


Figure 4. SEM images of ultralarge porous carbons after pyrolysis at 900  $^{\circ}$ C. (a–c) SEM image set of ULPC-1 formed from ULMM-SA1 coassembling with resols in a 7:3 (by mass) mixture of THF:EA; (d–f) SEM image set of ULPC-2 formed from ULMM-SA2 coassembling with resols in a 6:4 (by mass) mixture of THF:EA. Decreasing magnifications from left to right for both series illustrate the degree of homogeneity of the resulting co-continuous structures achieved across the entire sample.

EA content increases and decreases for PDMAEMA as EA content increases. From this, it was inferred that the way to minimize all radii for the blocks of the BCP and the resols additive is to have a mixture somewhere in the middle, that is near 50:50 in THF:EA, by mass. However, since group contribution methods were used in determining the solubility parameters for the PDMAEMA and resols, they cannot be relied on solely.<sup>46</sup> Furthermore, Hansen solubility parameters, as well as the Hildebrand solubility parameter, have no terms to account for variables such as temperature, concentration, or polymer molar mass, meaning that they are not 100% accurate.<sup>53</sup> Therefore, this qualitative modeling insight was combined with the empirical experimental results of the solvent ratios that produced the most desirable ULPC morphologies with co-continuous pore structure (e.g., see SEM in Figure 2, lower right) for the two BCPs ULMM-SA1 and ULMM-SA2. For preparing solutions of ULMM-SA1 and ULMM-SA2 with resols, the ideal solvent mass ratios were 7:3 THF:EA and 6:4 THF:EA, respectively. For illustration, Figure 3b-d shows SEM images of the porous structure of carbons after pyrolysis at 900 °C derived from ULMM-SA2 in THF, EA, and a mixture of the two solvents with a 6:4 THF:EA mass ratio, respectively. Images in Figure 3b,c suggest that when either THF or EA is used as a single solvent, micellization is a dominant assembly pathway during structure formation in the system of ULMM-SA co-assembling with phenol-formaldehyde resols. Since spherical carbon morphologies are ubiquitous in such samples, micelles are likely formed from PDMAEMA plus resols in the micelle core and PS chains forming the micelle corona. In contrast, the image in Figure 3d suggests that the assembly pathway switches when moving over to 6:4 THF:EA mass ratio mixtures, leading to the desired cocontinuous morphology after high-temperature treatment with continuous carbon and pore networks throughout the final

Multiple other strategies were employed to avoid micellization, in addition to tuning solvent system conditions. First, the BCPs were freeze-dried to remove any trace water from the hygroscopic PDMAEMA block. Water is much more polar than THF and EA, and it is a nonsolvent for polystyrene, meaning any ambient water in the polymer matrix could vastly impact the morphology and cause micellization during self-assembly. Second, during EISA the evaporation rate was

slowed by placing a glass dome over the dish with the evaporating sample, as well as including an additional solvent reservoir of THF next to the sample. This would saturate the local environment under the glass dome with the solvents in the vapor phase as the relatively volatile solvents evaporated, slowing down evaporation. This slower evaporation allowed the BCP to be solvent-enriched for a longer time as EISA took place, making it less likely that the BCP would get kinetically trapped in an unwanted morphology by one of the blocks becoming glassy before equilibrium was reached due to a lack of solvent. Since THF was the majority solvent for both ULMM-SA1 and 2, for simplicity we just added one additional solvent reservoir.

One final strategy was the order of how the components were added. The polymer was first dissolved into a 4 wt % solution of THF and EA in the desired ratio. This was allowed to mix for 6–12 h until the polymer was fully dissolved. Resols were added only after the polymer was fully dissolved in solution, and then the entire solution was diluted to a total of 4 wt % solids, while keeping the same THF:EA weight ratio. The resultant solution was then mixed for an additional 12 h. Mixing all components at once caused unwanted changes to the morphology, likely due to the fact that hydrogen-bonding effects between the resols and the PDMAEMA block, and resulting early multivalent BCP-resols interactions, would prevent reaching a fully solvated BCP in solution.

3.3. Pyrolysis into Co-continuous Ultralarge Porous Carbon Monoliths and Their Properties. Figure 4 shows SEM images of each ULPC after pyrolysis at 900 °C at varying magnifications, revealing the degree of homogeneity in the cocontinuous mesostructure achieved across both samples. By qualitatively comparing the observed pore sizes to the scale bars, it is clear that in both cases pores sizes are quite large, pushing well into the macropore regime (i.e., pore sizes >50 nm). The 3D co-continuous nature of the carbons allowed for isotropic shrinkage, letting the organic-organic hybrid films maintain their monolithic form through pyrolysis into the final carbon films. This is an important feature already observed in earlier studies with co-continuous carbons with gyroidal morphology, as it is a prerequisite, e.g., for the fabrication of 3D battery devices. The SEMs in Figure 4 further reveal thick pore walls, suggesting that higher-surface-area carbons could be achieved, e.g., by carbon activation to enhance micro-

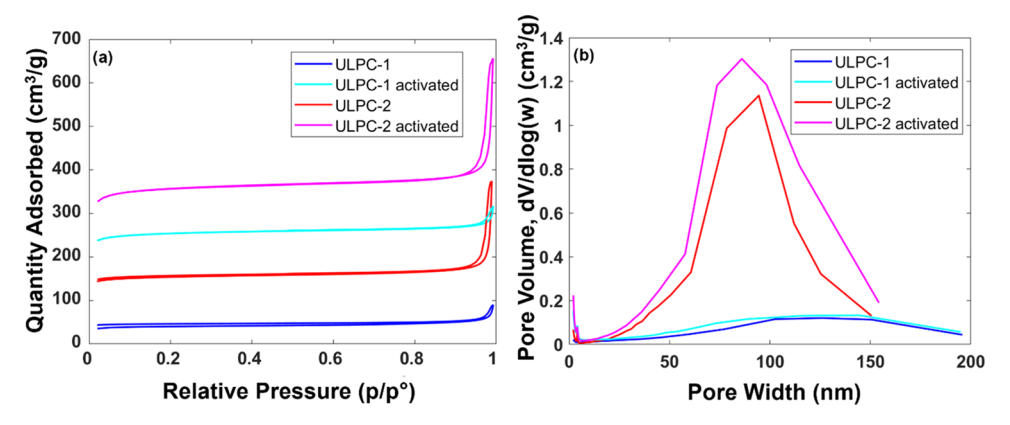
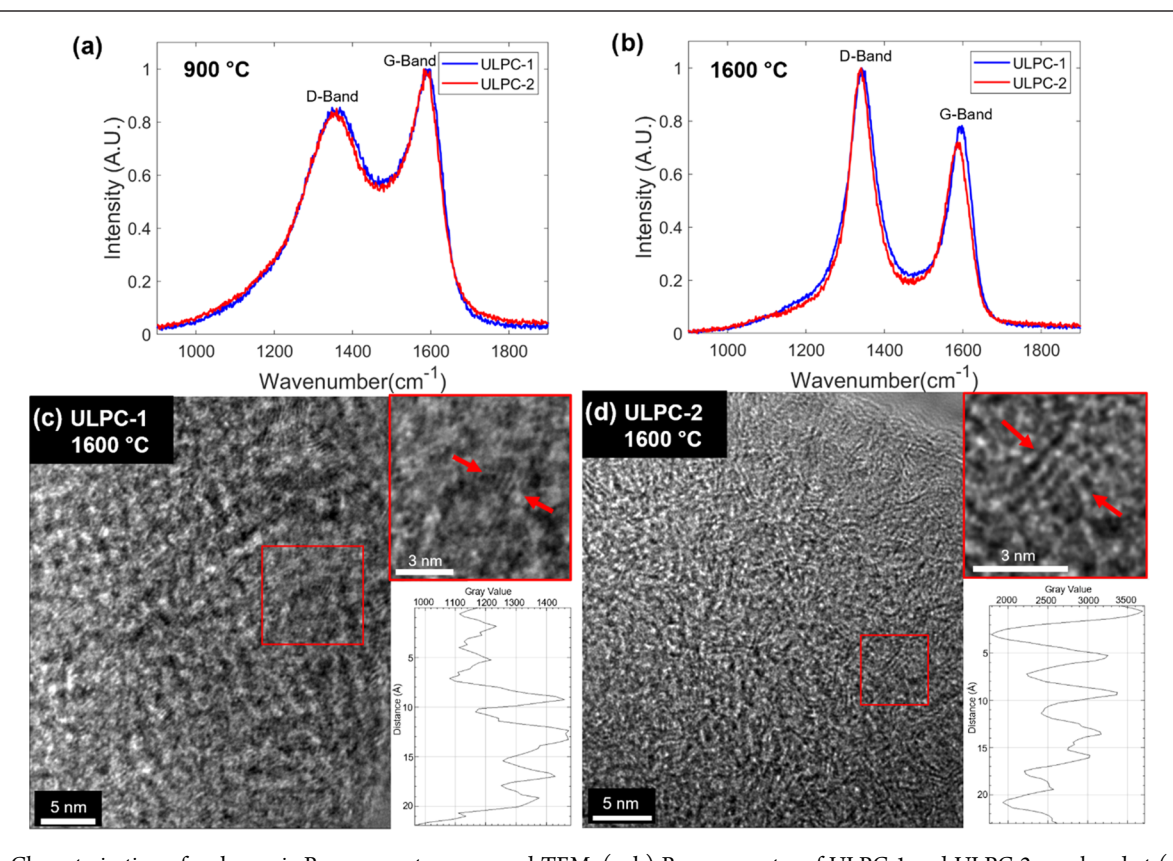


Figure 5. Nitrogen physisorption analysis of ULPC-1 and ULPC-2 pyrolyzed at 900 °C as well as after their respective 2 h carbon activation at 800 °C. (a) Isotherms for ULPC-1 and ULPC-2, as well as activated counterparts; (b) pore-size distributions for ULPC-1 and ULPC-2, as well as activated counterparts, from the desorption branches of the isotherms shown in (a).



**Figure 6.** Characterization of carbons via Raman spectroscopy and TEM. (a, b) Raman spectra of ULPC-1 and ULPC-2 pyrolyzed at (a) 900 °C and (b) 1600 °C, with the increased definition of the D- and G-bands from 900 to 1600 °C, indicating an increase in graphitic cluster size. (c, d) HR-TEM images of (c) ULPC-1 and (d) ULPC-2 pyrolyzed at 1600 °C, with insets zoomed in to highlight graphitic clusters on the order of the size predicted by Raman spectroscopy, as well as line graphs of grayscale intensity across the clusters of graphitic sheets showing peak-to-peak distances of approximately 3–4 Å.

porosity while maintaining the integrity of the co-continuous monolith structure; in turn, this could open up these carbon materials to applications such as supercapacitors. To that end, carbons pyrolyzed at 900 °C were further activated at 800 °C under a carbon dioxide (CO<sub>2</sub>) atmosphere for 2 h using protocols published earlier (see Experimental Methods) to see how the surface area would be impacted.<sup>2</sup>

To quantitatively characterize the pore space of the carbons before and after activation, nitrogen physisorption was performed on the samples, yielding type IV isotherms with H1 hysteresis (Figure 5). The Brunauer–Emmett–Teller

(BET) theory was then used to yield a surface area, while the Barrett–Joyner–Halenda (BJH) method was used to determine a pore-size distribution from the desorption branch of the isotherms. Figure 5a shows the isotherms for ULPC-1 and ULPC-2 and for their activated counterparts. Overall, ULPC-2 showed higher nitrogen adsorption, and by extension higher surface area, than ULPC-1. This is consistent with Figure 5b showing that the average pore in ULPC-1 was larger than that in ULPC-2, resulting in lower surface area. From Figure 5b, an average pore size of around 125 nm for ULPC-1 and around 94 nm for ULPC-2 can be inferred. While

distributions were somewhat broad, in particular for ULPC-1 materials, this was expected from the nonuniformity of the pores in these nonperiodically ordered co-continuous ULPCs. The activated ULPCs in Figure 5b showed similar average pore sizes and wide pore-size distributions as their nonactivated parents, but they also had notably larger contributions to pore volume from the microporous regime of pore size than their nonactivated counterparts. The isotherms for ULPC-1 and ULPC-2 were not closed where the adsorption and desorption branches typically meet at low relative pressure. This was likely due to the wide pore-size distribution and nonuniformity of the meso- to macropores, as well as potential ink-bottle pores in the carbon causing uneven rates of adsorption and desorption.<sup>56</sup> BET analysis of the isotherms revealed that ULPC-1 and ULPC-2 had specific surface areas (SSA) of 137 and 520 m<sup>2</sup>/g, respectively. The activated samples of both ULPC-1 and ULPC-2 had significantly increased surface areas of 858 and 1208 m<sup>2</sup>/g, respectively; the specific surface areas of both ULPCs increased by approximately 700 m<sup>2</sup>/g, indicating that the thick carbon walls from both samples activated at similar rates. It is also interesting to note that both of the isotherms for the activated samples were closed where the adsorption and desorption isotherms meet at low relative pressures. This could be due to activation eating into the walls of the carbons and opening up previous ink-bottle pores or activation making the percentage of surface area from micropores so dominant that any effects from uneven sorption rates from a wide distribution of meso- to macropores were overcome.

To investigate the graphitic nature of the ULPCs, Raman spectroscopy, transmission electron microscopy (TEM), X-ray photoelectron spectroscopy (XPS), X-ray diffraction (XRD), and conductivity measurements were performed. Figure 6 shows an ensemble of the results of the carbon structure and property characterization. Figure 6a depicts Raman spectra of ULPC-1 and ULPC-2 pyrolyzed at 900 °C, exhibiting the disordered band (D-band) and graphitic band (G-band). In disordered carbon materials, these D- and G-bands are typically located at approximately 1350 and 1590 cm<sup>-1</sup> respectively.<sup>57</sup> In ULPC-1, D- and G-bands were centered around 1368 and 1587 cm<sup>-1</sup>, respectively, while in ULPC-2, they were at 1352 and 1594 cm<sup>-1</sup>, respectively. The ratios of the integrated intensities of the fits for these bands were used to estimate in-plane graphitic cluster size via an empirical formula proposed by Tuinstra and Koenig (eq S1, Figure S3). 13,57,58 Not unexpected for this thermal treatment, ULPC-1 and ULPC-2 had similar cluster sizes of approximately only 1.7 and 1.8 nm, respectively.

Samples were further pyrolyzed up to 1600 °C to investigate if the graphitic quality could be improved. The original pyrolysis temperature of 900 °C was chosen as it is a common temperature for pyrolysis of carbon precursors into graphitic carbons, while 1600 °C was chosen to (i) demonstrate the robustness of the carbon monolith due to the thick pore walls and (ii) investigate improvements in electrochemical properties with increased pyrolysis temperature. The average pore size of carbons derived from resols structure directed via BCPs is not expected to be significantly impacted by the pyrolysis temperature. The average pore size of carbons derived from resols structure directed via BCPs is not expected to be significantly impacted by the pyrolysis temperature. The average pore size of carbons derived from resols structure directed via BCPs is not expected to be significantly impacted by the pyrolysis temperature. The average pore size of carbons derived from resols structure directed via BCPs is not expected to be significantly impacted by the pyrolysis temperature. The average pore size of carbons derived from resols structure directed via BCPs is not expected to be significantly impacted by the pyrolysis temperature. The average pore size of carbons derived from resols structure directed via BCPs is not expected to be significantly impacted by the pyrolysis temperature. The average pore size of carbons derived from resols structure directed via BCPs is not expected via BCPs.

nm for ULPC-1 and ULPC-2, respectively. Figure 6c,d shows high-resolution transmission electron microscopy (HR-TEM) images of ULPC-1 and ULPC-2, respectively, pyrolyzed at 1600  $^{\circ}$ C, in which these graphitic clusters can be easily identified. Insets in these figures zoom in on clusters of stacked in-plane graphitic sheets with periodicities of 3–4 Å and sizes consistent with those predicted by analysis of the corresponding Raman spectra in Figure 6b.

XPS was used to elucidate oxygen content at the surface of the materials that were pyrolyzed at 900 °C. By XPS elemental survey scans (Figure S4), ULPC-1 and ULPC-2 brought to 900 °C had surface oxygen atomic contents of 5.7 and 2.7%, respectively. XPS only penetrates about 10 nm into a sample, so it cannot be concluded that this result is representative of the oxygen content for the entirety of the thick bulk carbon pore walls of the ULPCs. However, as electrochemical processes occur at surfaces and interfaces, the oxygen content of the surface region 10 nm deep into the pore walls is more relevant than that of the deeper "bulk" of the materials. Highresolution XPS of the carbon edge for ULPC-1 and ULPC-2 pyrolyzed at 900 °C showed a large peak at ~284 eV with a trailing tail toward higher binding energy, which is indicative of sp<sup>2</sup>-hybridized carbon (Figure S5). XRD was used on the carbons pyrolyzed at 900 °C to elucidate the in-plane distance between graphitic sheets using the signal from the (200) peak, which is typically found at  $2\theta = 23-27^{\circ}$  in carbon materials when using Cu K $\alpha$  radiation (corresponding to q = 1.63-1.91Å-1); this should be approximately the C-C van der Waals distance, 0.34 nm (Figure S6). ULPC-1 and ULPC-2 both had (200) peaks at  $q = 1.63 \text{ Å}^{-1}$ , which corresponds to a spacing of 3.8 Å (corroborating the results from HR-TEM line graphs in Figure 6c,d). The full-width at half-maximum (FWHM) of the (200) peaks can also give information about the number of stacked graphitic sheets using the Scherrer equation to determine stack thickness. The FWHM for the (200) peaks of ULPC-1 and ULPC-2 were both 0.63 Å<sup>-1</sup>. This corresponds to stacks of about 9 Å thickness, indicating small stacks of about 2-3 sheets (thickness divided by the distance between sheets). This is less than the number of sheets suggested by cluster size analysis of the Raman spectroscopy results and supported by HR-TEM (6-7 sheets by counting the line graphs in Figure 6c,d), although no efforts were made to perform a more representative analysis by averaging over a larger number of such clusters observed by TEM. As another test to indicate the quality of the carbon samples, we performed 4-point probe conductivity measurements, since conductivity is an important characteristic for any material to be used in EES applications. The conductivities of ULPC-1 and ULPC-2 pyrolyzed at 900 °C were measured to be 0.52 Siemens per centimeter (S/cm) and 0.74 S/cm, respectively, consistent with such measurements on gyroidal mesoporous carbons in the past. 13 ULPC-1 and ULPC-2, when pyrolyzed at 1600 °C, had measured conductivities of 1.40 and 1.66 S/ cm, respectively, showing, as expected, increased electric conductivity with increased pyrolysis temperature.

#### 4. CONCLUSIONS

This work described the synthesis and characterization of ultralarge pore size graphitic carbon (ULPC) monoliths with co-continuous network morphology and pore sizes around 100 nm, derived from two ultralarge ( $\sim$ 1 M kDa) molar mass (ULMM) amphiphilic diblock copolymers. To that end, we used a self-assembly-based synthesis approach comprising an

ULMM BCP, PS-b-PDMAEMA, phenol-formaldehyde resols as carbon precursors, and a mixture of two solvents, THF and EA. The composition of the solvent mixture was fine-tuned, guided by a Hanson solubility parameter analysis, to minimize a micellization pathway and favor co-continuous structure formation of resols and amphiphilic BCP on the way to the final condensed phase structure obtained via EISA. Final porous materials were obtained via simple pyrolysis of the asmade composites at high temperatures (900 or 1600 °C, respectively) under an inert atmosphere. Under these conditions, rather than falling apart into many pieces, coherent monoliths could be obtained, likely due to the co-continuous structure of the porous carbons. Pore surface areas of the resulting materials could be elevated from hundreds of m<sup>2</sup>/g to values above 1000 m<sup>2</sup>/g by regular carbon activation procedures, leading to enhanced microporosity in the thick carbonaceous walls. The 3D co-continuous carbon and pore network structures of these ULPCs make them appealing for applications that require fast kinetics through the large 3D continuous pore network or backfilling processes, e.g., required for producing 3D nanoarchitecture-based EES devices.

#### ASSOCIATED CONTENT

#### Supporting Information

The Supporting Information is available free of charge at https://pubs.acs.org/doi/10.1021/acs.chemmater.1c01987.

Static light scattering analysis; proton nuclear magnetic resonance (NMR); estimates of the degree of polymerization for each block of ULMM-SA1 and ULMM-SA2; Raman spectroscopy fitting and analysis; X-ray photoelectron spectroscopy (XPS) data; X-ray diffraction (XRD) data (PDF)

## AUTHOR INFORMATION

# **Corresponding Author**

Ulrich B. Wiesner — Department of Materials Science & Engineering, Cornell University, Ithaca, New York 14853, United States; orcid.org/0000-0001-6934-3755; Email: ubw1@cornell.edu

# Authors

- William R. T. Tait Robert Frederick Smith School of Chemical and Biomolecular Engineering, Ithaca, New York 14853, United States; Department of Materials Science & Engineering, Cornell University, Ithaca, New York 14853, United States; orcid.org/0000-0001-8932-9416
- R. Paxton Thedford Robert Frederick Smith School of Chemical and Biomolecular Engineering, Ithaca, New York 14853, United States; Department of Materials Science & Engineering, Cornell University, Ithaca, New York 14853, United States; orcid.org/0000-0003-0811-227X
- Dana V. Chapman Department of Materials Science & Engineering, Cornell University, Ithaca, New York 14853, United States; Occid.org/0000-0002-9605-1886
- Fei Yu Department of Materials Science & Engineering, Cornell University, Ithaca, New York 14853, United States; Department of Chemistry and Chemical Biology, Cornell University, New York 14853, United States; ◎ orcid.org/ 0000-0002-8191-8096
- Judson W. Freidl Robert Frederick Smith School of Chemical and Biomolecular Engineering, Ithaca, New York 14853, United States

Ekaterina S. Sablina – Department of Materials Science & Engineering, Cornell University, Ithaca, New York 14853, United States

Gavin M. Batsimm – Robert Frederick Smith School of Chemical and Biomolecular Engineering, Ithaca, New York 14853, United States; © orcid.org/0000-0002-0184-5342

Complete contact information is available at: https://pubs.acs.org/10.1021/acs.chemmater.1c01987

#### **Author Contributions**

W.R.T.T. and R.P.T. contributed equally to this work.

#### Note

The authors declare no competing financial interest.

## ACKNOWLEDGMENTS

This work was funded by the U.S. Department of Energy, Office of Science, Basic Energy Sciences (DE-SC0010560). R.P. Thedford and D.V. Chapman were supported by the National Science Foundation (NSF) Graduate Research Fellowship Program under grant number DGE-1650441. This work made use of the Cornell Center for Materials Research shared facilities, which are supported by the NSF MRSEC program (DMR-1719875). This work made use of the Cornell University NMR Facility, which is supported, in part, by the NSF through MRI award CHE-1531632. This research also used the Soft Matter Interfaces beamline (12-ID) of the National Synchrotron Light Source II, a US Department of Energy (DOE) Office of Science User Facility operated for the DOE Office of Science by the Brookhaven National Laboratory under Contract no. DE-SC0012704.

# **■** REFERENCES

- (1) Ji, X.; Lee, K. T.; Nazar, L. A highly ordered nanostructured carbon-sulphur cathode for lithium-sulphur batteries. *Nat. Mater.* **2009**, *8*, 500–506.
- (2) Werner, J. G.; Johnson, S. S.; Vijay, V.; Wiesner, U. Carbon-sulfur composites from cylindrical and gyroidal mesoporous carbons with tunable properties in lithium-sulfur batteries. *Chem. Mater.* **2015**, 27, 3349–3357.
- (3) Carriazo, D.; Pico, F.; Gutierrez, M. C.; Rubio, F.; Rojo, J. M.; del Monte, F. Block-copolymer assisted synthesis of hierarchical carbon monoliths suitable as supercapacitor electrodes. *J. Mater. Chem.* **2010**, 20, 773–780.
- (4) Dickinson, A. J.; Carrette, L. P. I.; Collins, J. A.; Friedrich, K. A.; Stimming, U. Preparation of a Pt Ru/C catalyst from carbonyl complexes for fuel cell applications. *Electrochim. Acta* **2002**, *47*, 3733–3739.
- (5) Rolison, D. R.; Long, J. W.; Lytle, J. C.; Fischer, A. E.; Rhodes, C. P.; McEvoy, T. M.; Bourg, M. E.; Lubers, A. M. Multifunctional 3D nanoarchitectures for energy storage and conversion. *Chem. Soc. Rev.* **2009**, *38*, 226–252.
- (6) Long, J. W.; Dunn, B.; Rolison, D. R.; White, H. S. Three-dimensional battery architectures. *Chem. Rev.* **2004**, *104*, 4463–4492.
- (7) Werner, J. G.; Rodriguez-Calero, G. G.; Abruna, H. D.; Wiesner, U. Block copolymer derived 3-D interpenetrating multifunctional gyroidal nanohybrids for electrical energy storage. *Energy Environ. Sci.* **2018**, *11*, 1261–1270.
- (8) Penmatsa, V.; Kawarada, H.; Wang, C. Fabrication of carbon nanostructures using photo-nanoimprint lithography and pyrolysis. *J. Micromech. Microeng.* **2012**, 22, No. 045024.
- (9) Thurn-Albrecht, T.; Schotter, J.; Kastle, G. A.; Emley, N.; Shibauchi, T.; Krusin-Elbaum, L.; Guarini, K.; Black, C. T.; Tuominen, M. T.; Russell, T. P. Ultrahigh-density nanowire arrays grown in self-assembled diblock copolymer templates. *Science* **2000**, 290, 2126–2129.

- (10) Joo, S. H.; Choi, S. J.; Oh, I.; Kwak, J.; Liu, Z.; Terasaki, O.; Ryoo, R. Ordered Nanoporous arrays of carbon supporting high dispersions of platinum nanoparticles. *Nature* **2001**, 412, 169–172.
- (11) Templin, M.; Franck, A.; Du Chesnem, A.; Leist, H.; Zhang, Y.; Ulrich, R.; Schadler, V.; Wiesner, U. Organically modified aluminosilicate mesostructures from block copolymer phases. *Science* **1997**, 278, 1795–1798.
- (12) Ryoo, R. Synthesis of Highly Ordered Carbon Molecular Sieves via Template-Mediated Structural Transformation. *J. Phys. Chem. B.* **1999**, *103*, 7743–7746.
- (13) Werner, J. G.; Hoheisel, T. N.; Wiesner, U. Synthesis and characterization of gyroidal mesoporous carbons and carbon monoliths with tunable ultralarge pore size. *ACS Nano* **2014**, *8*, 731–743.
- (14) Tanaka, S.; Nishiyama, N.; Egashira, Y.; Ueyama, K. Synthesis of ordered mesoporous carbons with channel structure from an organic—organic nanocomposite. *Chem. Commun.* **2005**, 2125–2127.
- (15) Meng, Y.; Gu, D.; Zhang, F.; Shi, Y.; Yang, H.; Li, Z.; Yu, C.; Tu, B.; Zhao, D. Ordered mesoporous polymers and homologous carbon frameworks: amphiphilic surfactant templating and direct transformation. *Angew. Chem., Int. Ed.* 2005, 44, 7053–7059.
- (16) Meng, Y.; Gu, D.; Zhang, F. Q.; Shi, Y. F.; Cheng, L.; Feng, D.; Wu, Z. X.; Chen, Z. X.; Wan, Y.; Stein, A.; Zhao, D. A family of highly ordered mesoporous polymer resin and carbon structures from organic—organic self-assembly. *Chem. Mater.* **2006**, *18*, 4447–4464.
- (17) Deng, Y.; Yu, R.; Wan, X.; Shi, Y.; Meng, Y.; Gu, D.; Zhang, L.; Huang, Y.; Liu, C.; Wu, X.; Zhao, D. Ordered Mesoporous Silicas and Carbons with Large Accessible Pores Templated from Amphiphilic Diblock Copolymer Poly(ethylene oxide)-b-polystyrene. *J. Am. Chem. Soc.* 2007, 129, 1690–1697.
- (18) Zhang, J.; Deng, Y.; Wei, J.; Sun, Z.; Gu, D.; Bongard, H.; Liu, C.; Wu, H.; Tu, B.; Schüth, F.; Zhao, D. Design of amphiphilic ABC triblock copolymer for templating synthesis of large-pore ordered mesoporous carbons with tunable pore wall thickness. *Chem. Mater.* **2009**, *21*, 3996–4005.
- (19) Liu, L. W.; Wang, F.-Y.; Shao, G.-S.; Ma, T.-Y.; Zhong, Z.-Y. Synthesis of ultra-large mesoporous carbons from triblock copolymers and phloroglucinol/formaldehyde polymer. *Carbon* **2010**, *48*, 2660–2664
- (20) Wei, J.; Deng, Y.; Zhang, J.; Sun, Z.; Tu, B.; Zhao, D. Y. Large-pore ordered mesoporous carbons with tunable structures and pore sizes templated from poly (ethylene oxide)-b-poly (methyl methacrylate). *Solid State Sci.* **2011**, *13*, 784–792.
- (21) Zhang, Q.; Matsuoka, F.; Suh, H. S.; Beaucage, P. A.; Xiong, S.; Smilgies, D. M.; Tan, K. K.; Werner, J. G.; Nealey, P. F.; Wiesner, U. Pathways to mesoporous resin/carbon thin films with alternating gyroid morphology. *ACS Nano* **2018**, *12*, 347–358.
- (22) Hesse, S. A.; Werner, J. G.; Wiesner, U. One-Pot Synthesis of Hierarchically Macro-and Mesoporous Carbon Materials with Graded Porosity. *ACS Macro Lett.* **2015**, *4*, 477–482.
- (23) Liang, C. D.; Dai, S. Dual phase separation for synthesis of bimodal meso-/macroporous carbon monoliths. *Chem. Mater.* **2009**, 21, 2115–2124.
- (24) Mun, Y.; Jo, C.; Hyeon, T.; Lee, J.; Ha, K.-S.; Jun, K.-W.; Lee, S.-H.; Hong, S.-W.; Lee, H. I.; Yoon, S.; Lee, J. Simple synthesis of hierarchically structured partially graphitized carbon by emulsion/block-copolymer co-template method for high power supercapacitors. *Carbon* 2013, 64, 391–402.
- (25) Huang, Y.; Cai, H.; Feng, D.; Gu, D.; Deng, Y.; Tu, B.; Wang, H.; Webley, P. A.; Zhao, D. One-step hydrothermal synthesis of ordered mesostructured carbonaceous monoliths with hierarchical porosities. *Chem. Commun.* **2008**, 2641–2643.
- (26) Septani, C. M.; Wang, C.-A.; Jeng, U.-S.; Su, Y.-C.; Ko, B.-T.; Sun, Y.-S. Hierarchically Porous Carbon Materials from Self-Assembled Block Copolymer/Dopamine Mixtures. *Langmuir* **2020**, 36, 11754–11764.
- (27) Liu, H.; Wei, C.; Peng, L.; Fan, Q.; Matindi, C.; Wang, Y.; Ma, C.; Shi, J. High-effective preparation of 3D hierarchical nanoporous interpenetrating network structure carbon membranes as flexible free-

- standing anodes for stable lithium and sodium storage. *Colloids Surf.,* A 2021, 608, No. 125593.
- (28) Floudas, G.; Vazaiou, B.; Schipper, F.; Ulrich, R.; Wiesner, U.; Iatrou, H.; Hadjichristidis, N. Poly(ethylene oxide-b-isoprene) Diblock Copolymer Phase Diagram. *Macromolecules* **2001**, *34*, 2947–2957.
- (29) Ergang, N. S.; Fierke, M. A.; Wang, Z.; Smyrl, W. H.; Stein, A. Fabrication of a fully infiltrated three-dimensional solid-state interpenetrating electrochemical cell. *J. Electrochem. Soc.* **2007**, *154*, A1135.
- (30) Rhodes, C. P.; Long, J. W.; Pettigrew, K. A.; Stroud, R. M.; Rolison, D. R. Architectural integration of the components necessary for electrical energy storage on the nanoscale and in 3D. *Nanoscale* **2011**, *3*, 1731–1740.
- (31) Zhang, H.; Yu, X.; Braun, P. V. Three-dimensional bicontinuous ultrafast-charge and -discharge bulk battery electrodes. *Nat. Nanotechnol.* **2011**, *6*, 277–281.
- (32) Pikul, J. H.; Zhang, H. G.; Cho, J.; Braun, P. V.; King, W. P. High-power lithium ion microbatteries from interdigitated three-dimensional bicontinuous nanoporous electrodes. *Nat. Commun.* **2013**, *4*, No. 1732.
- (33) Hashimoto, T.; Shibayama, M.; Kawai, H. Domain-Boundary Structure of Styrene-Isoprene Block Copolymer Films Cast from Solution. 4. Molecular-Weight Dependence of Lamellar Microdomains. *Macromolecules* **1980**, *13*, 1237–1247.
- (34) Schacher, F.; Rudolph, T.; Wieberger, F.; Ulbricht, M.; Muller, A. H. E. Double Stimuli-Responsive Ultrafiltration Membranes from Polystyrene-block-poly(N,N-dimethylaminoethyl methacrylate) Diblock Copolymers. ACS Appl. Mater. Interfaces 2009, 1, 1492–1503.
- (35) Sveinbjornsson, B. R.; Weitekamp, R. A.; Miyake, G. M.; Xia, Y.; Atwater, H. A.; Grubbs, R. H. Rapid self-assembly of brush block copolymers to photonic crystals. *Proc. Natl. Acad. Sci. USA* **2012**, *109*, 14332–14336.
- (36) Yu, Y.-G.; Chae, C.-G.; Kim, M.-J.; Seo, H.-B.; Grubbs, R. H.; Lee, J.-S. Precise Synthesis of Bottlebrush Block Copolymers from  $\omega$ -End-Norbornyl Polystyrene and Poly(4-tert-butoxystyrene) via Living Anionic Polymerization and Ring-Opening Metathesis Polymerization. *Macromolecules* **2018**, *51*, 447–455.
- (37) Fei, H.-F.; Long, Y.; Yu, H.-Y.; Yavitt, B. M.; Fan, W.; Ribbe, A.; Watkins, J. J. Bimodal Mesoporous Carbon Spheres with Small and Ultra-Large Pores Fabricated Using Amphiphilic Brush Block Copolymer Micelle Templates. ACS Appl. Mater. Interfaces 2020, 12, 57322–57329.
- (38) Fei, H.-F.; Li, W.; Bhardwaj, A.; Nugiri, S.; Ribbe, A.; Watkins, J. J. Ordered Nanoporous Carbons with Broadly Tunable Pore Size Using Bottlebrush Block Copolymer Templates. *J. Am. Chem. Soc.* **2019**, *141*, 17006–17014.
- (39) Park, S.; Kim, Y.; Ahn, H.; Kim, J. H.; Yoo, P. J.; Ryu, D. Y. Giant gyroid and templates from high-molecular-weight block copolymer self-assembly. *Sci. Rep.* **2016**, *6*, No. 36326.
- (40) Yoon, J.; Lee, W.; Thomas, E. L. Highly Oriented Thin-Film Microdomain Patterns of Ultrahigh Molecular Weight Block Copolymers via Directional Solidification of a Solvent. *Adv. Mater.* **2006**, *18*, 2691–2694.
- (41) Appold, M.; Gallei, M. Bio-Inspired Structural Colors Based on Linear Ultrahigh Molecular Weight Block Copolymers. *ACS Appl. Polym. Mater.* **2019**, *1*, 239–250.
- (42) Clayden, J.; Yasin, S. A. Pathways for decomposition of THF by organolithiums: the role of HMPA. *New J. Chem.* **2002**, *26*, 191–192.
- (43) Zimm, B. H. The scattering of light and the radial distribution function of high polymer solutions. *J. Chem. Phys.* **1948**, *16*, 1093–1099.
- (44) Cummins, C.; Alvarez-Fernandez, A.; Bentaleb, A.; Hadziioannou, G.; Ponsinet, V.; Fleury, G. Strategy for Enhancing Ultrahigh-Molecular-Weight Block Copolymer Chain Mobility to Access Large Period Sizes (>100 nm). *Langmuir* **2020**, *36*, 13872–13880
- (45) C. M., Hansen Hansen Solubility Parameters: A user's Handbook, 2nd ed.; CRC Press LLC: Boca Raton, Florida, 2007.

- (46) Wan, Y.; He, H.; Huang, Z.; Zhang, P.; Sha, J.; Li, T.; Ren, B. Solubility, thermodynamic modeling and Hansen solubility parameter of 5-norbornene-2,3-dicarboximide in three binary solvents (methanol, ethanol, ethyl acetate + DMF) from 278.15 K to 323.15 K. J. Mol. Liq. 2020, 300, No. 112097.
- (47) Özdemir, C.; Guner, A. Solubility profiles of poly(ethylene glycol)/solvent systems, I: Qualitative comparison of solubility parameter approaches. *Eur. Polym. J.* **2007**, *43*, 3068–3093.
- (48) Just, S.; Sievert, F.; Thommes, M.; Breitkreutz, J. Improved group contribution parameter set for the application of solubility parameters to melt extrusion. *Eur. J. Pharm. Biopharm.* **2013**, *85*, 1191–1199.
- (49) Garcia, B. C.; Kamperman, M.; Ulrich, R.; Jain, A.; Gruner, S. M.; Wiesner, U. Morphology Diagram of a Diblock Copolymer Aluminosilicate Nanoparticle System. *Chem. Mater.* **2009**, *21*, 5397–5405
- (50) De Paul, S. M.; Zwanziger, J. W.; Ulrich, R.; Wiesner, U.; Spiess, H. W. Structure, Mobility, and Interface Characterization of Self-Organized Organic-Inorganic Hybrid Materials by Solid-State NM. *J. Am. Chem. Soc.* **1999**, *121*, 5727–5736.
- (51) Simon, P. F. W.; Ulrich, R.; Spiess, H. W.; Wiesner, U. Review: Block copolymer ceramic hybrid materials from organically modified silicon precursors. *Chem. Mater.* **2001**, *13*, 3464–3486.
- (52) Lindvig, T.; Michelsen, M. L.; Kontogeorgis, G. M. A Flory—Huggins model based on the Hansen solubility parameters. *Fluid Phase Equilib.* **2002**, 203, 247–260.
- (53) Venkatram, S.; Kim, C.; Chandrasekaran, A.; Ramprasad, R. Critical Assessment of the Hildebrand and Hansen Solubility Parameters for Polymers. J. Chem. Inf. Model. 2019, 59, 4188–4194.
- (54) Stefik, M.; Song, J.; Sai, H.; Guldin, S.; Boldrighini, P.; Orilall, M. C.; Steiner, U.; Gruner, S. M.; Wiesner, U. Ordered mesoporous titania from highly amphiphilic block copolymers: tuned solution conditions enable highly ordered morphologies and ultra-large mesopores. *J. Mater. Chem. A* **2015**, *3*, 11478–11492.
- (55) Cychosz, K. A.; Guillet-Nicolas, R.; Garcia-Martinez, J.; Thommes, M. Recent advances in the textural characterization of hierarchically structured nanoporous materials. *Chem. Soc. Rev.* **2017**, 46, 389–414.
- (56) Qi, L.; Tang, X.; Wang, Z.; Peng, X. Pore characterization of different types of coal from coal and gas outburst disaster sites using low temperature nitrogen adsorption approach. *Int. J. Min. Sci. Technol.* **2017**, *27*, 371–377.
- (57) Ferrari, A. C.; Robertson, J. Interpretation of Raman spectra of disordered and amorphous carbon. *Phys. Rev. B* **2000**, *61*, 14095–14107.
- (58) Tuinstra, F.; Koenig, J. L. Raman spectrum of graphite. *J. Chem. Phys.* **1970**, 53, 1126–1130.